Soft Matter

PAPER
Matthias Karg *et al.*
Translational and rotational diffusion coefficients of gold nanorods functionalized with a high molecular weight, thermoresponsive ligand: a depolarized dynamic light scattering study

ROYAL SOCIETY
OF **CHEMISTRY**

PAPER

Check for updates

Translational and rotational diffusion coefficients of gold nanorods functionalized with a high molecular weight, thermoresponsive ligand: a depolarized dynamic light scattering study†

Déborah Feller, [ID] [a] Marius Otten, [a] Marco Hildebrandt, [a] Marcel Krüsmann, [a] Gary Bryant [ID] [b] and Matthias Karg [ID] *[a]

Probing the rotational and translational diffusion and colloidal stability of nanorods is of significant fundamental interest with implications for many different applications. Recently R. Nixon-Luke and G. Bryant presented a method to analyze angle-dependent depolarized dynamic light scattering data allowing for the clear separation of the translational and rotational diffusion coefficients of gold nanorods in dilute suspension (R. Nixon-Luke and G. Bryant, *Part. Part. Syst. Charact.*, 2018, **36**, 1800388). In the present work we applied this analysis to gold nanorods decorated with high molecular weight, thermoresponsive poly-*N*-isopropylacrylamide ligands, which results in particles with lower effective aspect ratios. The temperature response of the ligand shell is studied. We precisely determine the translational and rotational diffusion coefficients over a broad range of temperatures and the results are compared to theoretical predictions. The results show that as temperature increases the ligands collapse, and the effective aspect ratio increases as the particle shape transitions from prolate spheroid at low temperatures to more cylindrical at high temperatures.

1 Introduction

Noble metal nanoparticles play an important role in nanotechnology due to their unique electrical and optical properties.[2–4] Their interaction with light manifests in localized surface plasmon resonances (LSPRs) that result from the resonant excitation of the valence electrons by the oscillating electric field of the incident waves. Since these resonances are directly affected by parameters such as particle size, shape and composition, a lot of effort has been devoted to the synthesis of noble metal nanoparticles with defined morphologies. In particular in the field of gold nanoparticles, countless synthesis protocols have been reported with extraordinary control of particle size and shape with high yield and low dispersities.[5–9] For applications such as metamaterials, sensing and photothermal actuation, gold nanorods are particularly interesting as they support intense longitudinal LSPRs with a resonance wavelength and strength that depend on the rod length.[10] Simply through variation of the length, the longitudinal LSPR can be shifted from the red to the infrared spectral region.[11,12] Furthermore, gold nanorods are an ideal model system for anisotropic colloids as their aspect ratio can be adjusted over a broad range. To increase the colloidal stability and be able to remove the large excess of surfactant that is commonly used in the synthesis of gold nanorods, ligand exchange with end-functionalized polymers is a well suited approach. By ligand exchange it is also possible to provide nanoparticles with additional properties, for example if stimuli-responsive polymers are used as ligands.[13] These hybrid particles can yield new multifunctional materials that can exploit synergistic effects and/or feature new properties that neither of the individual components possess on their own. Along these lines gold nanoparticles have been combined with thermoresponsive polymers to allow for photothermal manipulation of the polymer *via* laser excitation of the plasmonic particles.[14,15] Conversely, conformational changes of thermoresponsive polymers can be used to trigger LSPR shifts of plasmonic particles.[16,17] In the special case of gold nanorods, thermoresponsive polymer ligands may allow for external manipulation of the effective aspect ratio *via* temperature, *i.e.* a smaller aspect ratio for good solvent conditions where the ligand shell is in an expanded state and a higher aspect ratio for bad solvent conditions where the ligand shell is collapsed onto the nanorod surface. These changes will ultimately affect the translational and rotational diffusion of the nanorods.

[a] *Physikalische Chemie I: Kolloide und Nanooptik, Heinrich-Heine-Universität Düsseldorf, 40225 Düsseldorf, Germany. E-mail: karg@hhu.de*
[b] *Physics, School of Science, RMIT University, Melbourne, Victoria 3001, Australia*
† Electronic supplementary information (ESI) available. See DOI: 10.1039/d1sm00077b

For isotropic particles in a dilute dispersion, diffusion is commonly studied by dynamic light scattering (DLS) yielding average relaxation times that can be directly used to determine the translational diffusion coefficient. For anisotropic particles, translational as well as rotational motions contribute to the autocorrelation function recorded in DLS. Thus, the determination of particle dimensions, *i.e.* the length and diameter, is not possible by standard DLS. For nanorods stabilized by polymer ligands, standard DLS can also not be used to measure the shell thickness that determines the effective aspect ratio of the particles. To decouple translational and rotational motion, depolarized DLS (DDLS) has been successfully applied to various systems like tobacco mosaic virus,[18] dumbbell-shaped polyelectrolyte brushes,[19] and gold nanorods,[1,20,21] among others.

In this work, we study gold nanorods that were surface functionalized with high molecular weight, thermoresponsive polymer ligands composed of poly-*N*-isopropylacrylamide (PNIPAM). The structure of the particles and their response to temperature is schematically illustrated in Scheme 1. DLS and DDLS were used to study the diffusion in dilute aqueous dispersion over a wide range of scattering angles and for temperatures below and close to the lower critical solution temperature (LCST) of the polymer ligand. This allowed for the determination of the rotational and translational diffusion coefficients as a function of temperature. The ligand thickness was estimated using the isotropic scattering of polymer decorated spherical gold nanoparticles as a reference system. This in turn could be used to calculate the effective aspect ratio of the polymer decorated nanorods. Our findings were compared to the theoretical prediction for prolate spheroids.
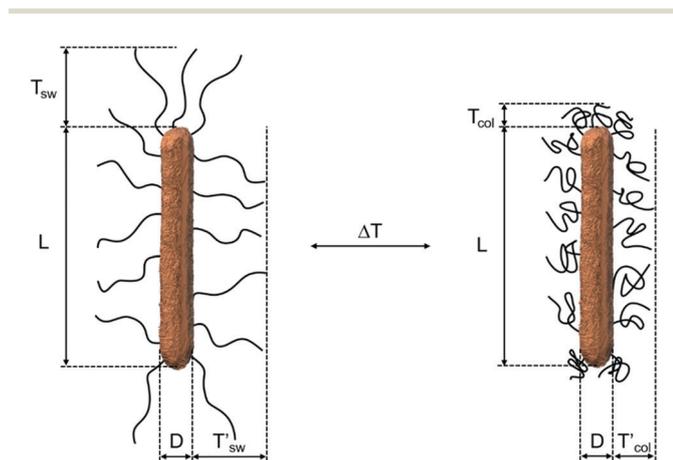
Scheme 1 Schematic illustration of a PNIPAM-decorated gold nanorod where the nanorod is a 3D reconstruction from a transmission electron microscopy tomography series. Here L refers to the rod length, D refers to the rod diameter. T and T' correspond to the ligand shell thicknesses at the tips and sides of the rods, respectively. The illustration on the left shows the ligand in the swollen state (index sw), *i.e.*, at temperatures below the LCST. The illustration on the right shows the ligand in the collapsed state (index col), *i.e.*, at temperatures above the LCST.

2 Theory

2.1 DLS

In DLS, the fluctuations of the scattering intensity are measured over time and converted into the intensity–time autocorrelation function $g^{(2)}(\tau)$.[22]

$$g^{(2)}(\tau) = \frac{\langle I(t)I(t+\tau)\rangle}{\langle I(t)\rangle^2} \quad (1)$$

where $\langle\rangle$ refers to the average of the scattering intensity over the time and $I(t)$ and $I(t+\tau)$ denote respectively the intensities of the scattered light at times t and $t+\tau$, where τ is the delay time. $g^{(2)}(\tau)$ can be converted into the electric field–time autocorrelation function, $g^{(1)}(\tau)$, using the Siegert relation:

$$g^{(2)}(\tau) = 1 + \beta|g^{(1)}(\tau)|^2 \quad (2)$$

here B denotes the value for the baseline and β refers to the intercept related to the signal-to-noise ratio.

For a dilute dispersion of monodisperse, isotropic scattering objects $g^{(1)}(\tau)$ follows a single exponential decay function:

$$g^{(1)}(\tau) = \exp(-\Gamma\tau) \quad (3)$$

where Γ is the decay or relaxation rate that is related to the translational diffusion coefficient D_t by:

$$\Gamma = D_t q^2 \quad (4)$$

where q the magnitude of the scattering vector $\vec{q}$:

$$|\vec{q}| = q = \frac{4\pi n}{\lambda}\sin\left(\frac{\theta}{2}\right) \quad (5)$$

here n denotes the refractive index of the dispersion medium, λ refers to the wavelength of the incident laser light and θ refers to the scattering angle, *i.e.*, the angle between the transmitted beam and the detector.

Using D_t the hydrodynamic radius R_H can be calculated by applying the Stokes–Einstein equation:

$$R_H = \frac{k_B T}{6\pi\eta D_t} \quad (6)$$

where k_B is the Boltzmann constant, T is the absolute temperature and η refers to the dynamic viscosity of the surrounding medium.

In this work all experiments were performed with incident laser light that is vertically linearly polarized. Measurements under two different polarization conditions were performed: (1) the polarizer in front of the detector is oriented vertically (VV measurement). This corresponds to a standard polarized DLS experiment. (2) The polarizer in front of the detector is oriented horizontally (H), the scattering is depolarized and is designated a VH measurement. This corresponds to a DDLS experiment.

2.1.1 Polarized DLS – VV geometry. For the polarized measurements, rotational as well as translational diffusion contributes to the fluctuations of the scattered light intensity. The corresponding electric field–time autocorrelation functions can be described by:[1]

$$g^{(1)}_{VV}(q,\tau) = S_0\exp(-D_t q^2\tau) + S_2\exp(-(D_t q^2 + 6D_r)\tau) \quad (7)$$

where S_i are coefficients calculated from a Legendre polynomial, D_t is the translational diffusion coefficient and D_r is the rotational diffusion coefficient.

By plotting $g_{VV}^{(1)}(q,\tau)$ against $q^2\tau$, it is possible to identify the range of scattering angles for which D_t can be reliably determined. For these scattering angles eqn (7) can be used to determine D_t.

2.1.2 Depolarized DLS – VH geometry. In the depolarized measurements, the value of D_r is constant over all the scattering angles, so applying $q^2\tau$ scaling is not required. The averaged value of D_t from the VV data is used as an input to calculate D_r directly from $g^{(2)}(\tau)$.[1]

$$g_{VH}^{(2)}(q,\tau) - 1 = \beta \exp(-2(q^2 D_t + 6D_r)\tau) \qquad (8)$$

2.2 Theoretical calculations of D_r and D_t

The theory of Tirado and Garcia de la Torre (TG)[23,24] is well-established to predict the diffusion coefficients of rod like particles which have an aspect ratio $p = L/D$ of $2 < p < 30$. While this theory should hold for our gold nanorod cores ($p \approx 6$), the PNIPAM ligand shell leads to a significant reduction of the effective aspect ratio ($p < 2$), where the TG theory is no longer applicable. For this reason, the theory established by Perrin for prolate ellipsoids is applied.[20,25]

The translational diffusion coefficient D_t is given by:

$$D_t = \frac{k_B T}{3\pi\eta L}F(p) \qquad (9)$$

where T is the absolute temperature, η is the viscosity of the medium and $F(p)$ is given by

$$F(p) = pS(p) \qquad (10)$$

with

$$S(p) = \frac{\ln\left(p + \sqrt{p^2 - 1}\right)}{\sqrt{p^2 - 1}} \qquad (11)$$

The rotational diffusion coefficient D_r is given by:

$$D_r = \frac{3k_B T}{\pi\eta L^3}G(p) \qquad (12)$$

with

$$G(p) = \frac{\frac{1}{2}p^2\left[\left(\frac{2p^2 - 1}{p}\right)S(p) - 1\right]}{(p^2 - 1)} \qquad (13)$$

Thus, by using the gold nanorod dimensions and estimates of the PNIPAM brush thickness it becomes possible to calculate theoretical diffusion coefficients.

3 Results and discussion

3.1 Determination of size and shape of the gold nanorods

In this work, two batches of gold nanorods (AuNRs) decorated with the same PNIPAM ligand (AuNR–PNIPAM) are analysed. The nanorods vary in their diameter D and length L. Fig. 1a and b
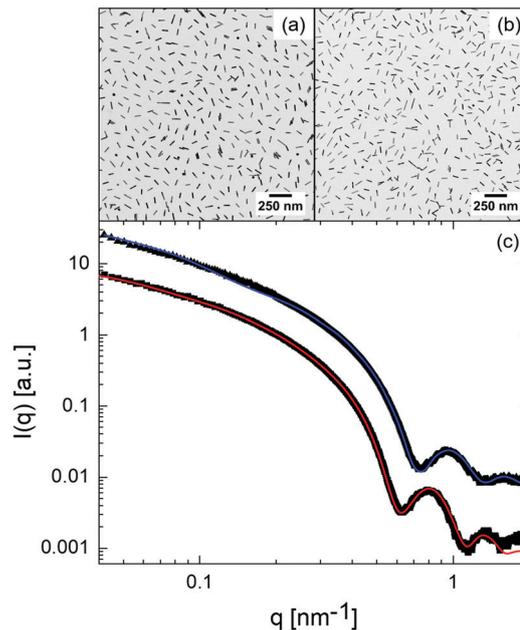

Fig. 1 Particle characterization by TEM and SAXS. Representative bright-field TEM images of AuNR–PNIPAM-1 (a) and AuNR–PNIPAM-2 (b). (c) SAXS profiles for AuNR–PNIPAM-1 (square symbols and red fit) and AuNR–PNIPAM-2 (triangles and blue fit). The data and fit of the AuNR–PNIPAM-2 sample were shifted vertically for clarity.

show selected bright-field TEM images of the respective AuNR–PNIPAM particles. Both samples confirm the high yield of near monodisperse nanorods with very few spherical particles. Additional images for both particle species recorded at low and high magnification as well as histograms for L and D determined from TEM are shown in the ESI,† Fig. S1–S6. Although drop-casting was used to prepare the samples, neither particle species agglomerated on the TEM grids upon drying. Both samples show a nearly constant separation between the particles. These observations can be explained by the steric hinderance of the polymer brushes during the drying process, even if the brushes collapse during this process. Further, as a result of the comparatively low contrast, the polymer brush is difficult to visualise – however, the collapsed polymer brushes on the AuNR surface can be seen in the higher magnification images shown in Fig. S3 and S6 in the ESI.† To determine the dimensions of the nanorod cores, 130 particles were measured for each sample. The core diameter and length for AuNR–PNIPAM-1 are 12.5 ± 0.8 nm and 76.0 ± 8.4 nm, respectively and for AuNR–PNIPAM-2 10.8 ± 0.9 nm and 65.7 ± 6.9 nm. The dimensions are also listed in Table 1 along with the resulting

Table 1 Length L, diameter D and aspect ratio p from TEM and SAXS

	AuNR–PNIPAM-1		AuNR–PNIPAM-2	
	TEM	SAXS	TEM	SAXS
L [nm]	76.0 ± 8.4	76.0 ± 3.7	65.7 ± 6.9	65.7 ± 3.0
D [nm]	12.5 ± 0.8	12.4 ± 0.6	10.8 ± 0.9	10.4 ± 0.6
Aspect ratio $p = L/D$	6.1 ± 1.0	6.1 ± 0.6	6.1 ± 1.2	6.3 ± 0.7

aspect ratios. Within the errors both AuNR samples possess the same aspect ratio (p = 6.1).

To also study the size, shape and stability of the AuNR–PNIPAM samples in dispersion and as an ensemble average, we performed small-angle X-ray scattering (SAXS) measurements. The resulting SAXS profiles in Fig. 2c show a pronounced form factor ($P(q)$) with several minima at high q values, which supports the low poly-dispersity observed by TEM. Because of the low X-ray scattering length density difference between PNIPAM and the dispersion medium (water) as compared to the high contrast of the AuNR, the SAXS profiles are dominated by scattering of the AuNR cores. It is not possible to resolve the PNIPAM brushes in these measurements. In order to describe the SAXS profiles, we applied the model for a long cylindrical particle (see ESI† for a detailed discussion and equations). To account for a small fraction of aggregates in the samples, contributing only at low q, a fractal contribution was added to the cylinder form factor. In general the obtained length L and diameter D from the cylinder model (see values in Table 1) are in good agreement with the values obtained from TEM. Small differences are ascribed to the much better statistics in SAXS compared to TEM measurements due to the

higher number of examined particles. Thus, in the following we will use the dimensions obtained from SAXS for further analysis.

The optical properties of the AuNR–PNIPAM samples were studied using UV/vis spectroscopy. Respective spectra are shown in Fig. S8 and S9 in the ESI.† Both samples feature a transverse LSPR at approximately 510 nm and longitudinal LSPRs at approximately 974 nm for AuNR–PNIPAM-1 and at 908 nm for AuNR–PNIPAM-2 at 15 °C. Increasing the temperature leads to a significant redshift of the longitudinal LSPR for both samples. This redshift is attributed to the increased local refractive index due to the collapse of the ligand shell confirming once more the success of the ligand exchange with the PNIPAM ligands.

3.2 DLS and DDLS measurements

We performed DLS and DDLS measurements at temperatures below and close to the LCST of the PNIPAM ligands over a wide range of scattering angles to precisely determine the translational and rotational diffusion coefficients.

3.2.1 Analysis of the VV-measurements. In a first step, the DLS measurements (VV) are used to obtain D_t at each investigated temperature. To do so, we first had to calculate the field–time autocorrelation functions $g_{VV}^{(1)}(q,\tau)$ from the measured $g_{VV}^{(2)}(q,\tau)$ using the Siegert–Relation (eqn (2)). The intercept β was determined by averaging the first 20 data points of $g_{VV}^{(2)}(q,\tau)$. The resulting $g_{VV}^{(1)}(q,\tau)$ curves for both samples measured at 25 °C are shown in Fig. 2a and b.

The decay of the correlation functions moves to shorter delay times τ with increasing scattering angle. At scattering angles from 20° to 60° (purple to blue), the curves show a clear bimodal decay behavior, while for larger angles the curves appear nearly monomodal. To precisely determine the translational diffusion coefficients from the DLS data, the correlation data are plotted as a function of $q^2\tau$ as shown in Fig. S10 and S12 in the ESI.† For homogeneous and isotropic scattering objects, it is expected that all curves collapse onto a master curve if plotted against $q^2\tau$. For our AuNR–PNIPAM particles this is clearly not the case. In this case both D_t and D_r contribute to the correlation functions. One can see that the long-time decay follows the expected scaling for translational diffusion at large enough scattering angles. Fig. 2c and d shows the selected correlation functions for scattering angles from 70° to 140° where the scaling is fulfilled. It should be noted that the first decay at short delay times does not collapse for any scattering angle, which is an indication that this decay is due to a combination of rotation and translation. The second decay at longer delay times is only caused by translational motion at these scattering angles. Therefore, only curves at these angles will be fitted using eqn (7) yielding values for D_t. The high quality of the fits is demonstrated by the examples in Fig. 2e and f, for correlation functions from a scattering angle of 120 °C. The corresponding fits match almost perfectly with the experimental curves. This observation is further confirmed by the calculated deviation between the experimental and fitted curves as shown in Fig. S11 and S13 in the ESI.†
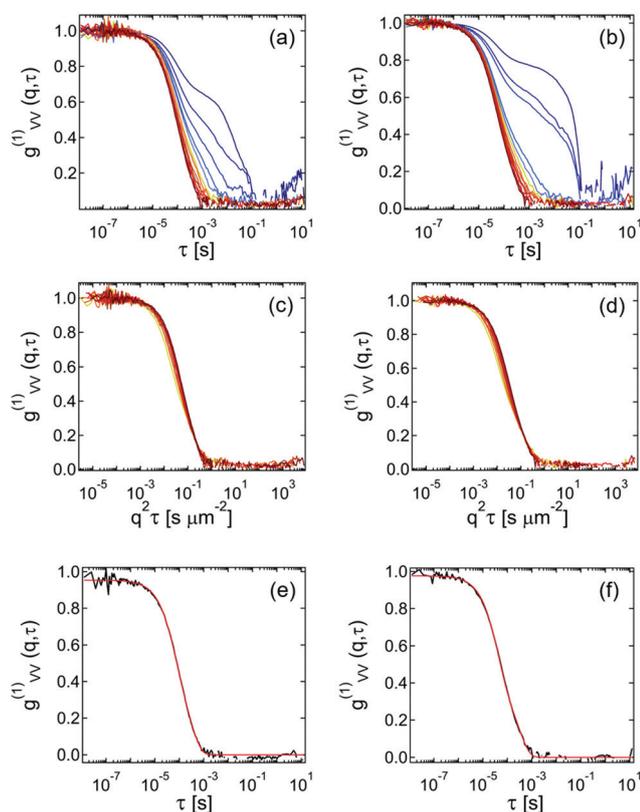

Fig. 2 Results from angle-dependent DLS experiments at 25 °C. $g_{VV}^{(1)}(q,\tau)$ for AuNR–PNIPAM-1 (a) and AuNR–PNIPAM-2 (b) at a range of scattering angles from 20° to 140° in steps of 10°. The scattering angle increases from blue to red. Selected $g_{VV}^{(1)}(q,\tau)$ plotted against $q^2\tau$ for AuNR–PNIPAM-1 (c) and for AuNR–PNIPAM-2 (d) only showing the range of angles where the long-time decay fully collapses onto a master curve. Example $g_{VV}^{(1)}(q,\tau)$ from 120° scattering angle (black lines) and fits using eqn (7) (red lines) for AuNR–PNIPAM-1 (e) and AuNR–PNIPAM-2 (f).
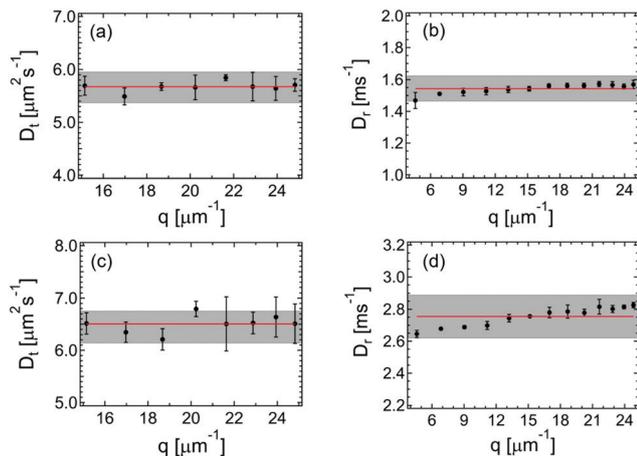
Fig. 3 Diffusion coefficients from DLS and DDLS measurements at 25 °C. D_t plotted against q for AuNR–PNIPAM-1 (a) and AuNR–PNIPAM-2 (c). D_r plotted against q for AuNR–PNIPAM-1 (b) and AuNR–PNIPAM-2 (d). The red lines indicate the average values of the respective diffusion coefficients for the whole q-range. The gray boxes in each plot represent an error range of 5% with respect to the average values of each coefficient.

The determined values of D_t are plotted as a function of q in Fig. 3a and c. As expected for translational diffusion of a highly dilute particle dispersion, nearly constant values of D_t were obtained over the whole q-range for both samples. Thus, in the following we will use the q-average values of D_t indicated by the red lines in Fig. 3a and c for analysis of the DDLS data. The average value of D_t is significantly higher for the AuNR–PNIPAM-2 particles because of their smaller length as compared to AuNR–PNIPAM-1 (see eqn (9)).

3.2.2 Analysis of the VH-measurements. Fig. 4a and b show the measured $g_{VH}^{(2)}(q,\tau) - 1$ curves for scattering angles between 20° and 140° in 10° steps for both samples. As the VH data do not need to be normalized in contrast to the VV data, $g_{VH}^{(2)}(q,\tau) - 1$ can be directly used for analysis. All curves show a monomodal decay and an almost negligible influence of the scattering angle indicating that the rotational motion is dominating the correlation functions.

To analyse the DDLS data, $g_{VH}^{(2)}(q,\tau) - 1$ was fitted using eqn (8) with the average value of D_t obtained from DLS measurements as a fixed parameter. The representative fits recorded at 120° scattering angle presented in Fig. 4c and d show only small deviations from the data, mostly at longer delay times. The deviation is calculated and shown in Fig. S14 and S15 in the ESI.† These small deviations are likely due to the (small) inherent polydispersity of the particles, which is not taken into account in this analysis.

The obtained values of D_r are plotted as a function of q in Fig. 3a and c. Despite a general trend of slightly increasing D_r with increasing q for both samples, the changes in D_r in the measured q-range are small (less than 5% from the average as indicated by the grey error corridors in Fig. 3). Thus, in the following we will use the q-average values of D_r for further analysis and discussion of temperature dependent data. Like the translational diffusion coefficient, the average value of D_r is significantly higher for the AuNR–PNIPAM-2 particles because

of their smaller length compared to AuNR–PNIPAM-1 (see eqn (12)).

3.2.3 Temperature induced shrinkage of the PNIPAM ligands. In the following we will investigate the influence of temperature on the PNIPAM brush thickness and its effect on translational and rotational diffusion (see Scheme 1 for a schematic illustration). To do so, angle-dependent DLS and DDLS measurements were performed for a broad range of temperatures below and close to the LCST of the PNIPAM ligands. The data were analysed to extract values of D_t and D_r as described in the previous two sections. It should be noted that measurements could not be performed at temperatures higher than 33 °C for AuNR–PNIPAM-1 and 35 °C for AuNR–PNIPAM-2 due to weak colloidal stability at temperatures significantly above the LCST. Fig. 5 summarizes the obtained diffusion coefficients. D_t (black circles) and D_r (red circles) both increase continuously with increasing temperature for the two samples. D_r increases by approximately a factor of two, significantly more than the change in D_t. These changes are consistent with the thermoresponsive behavior of the PNIPAM ligands that shrink with increasing temperature due to a change in solvent

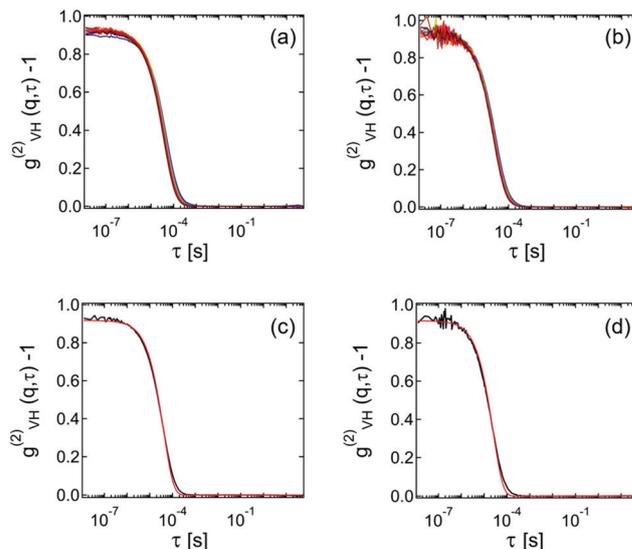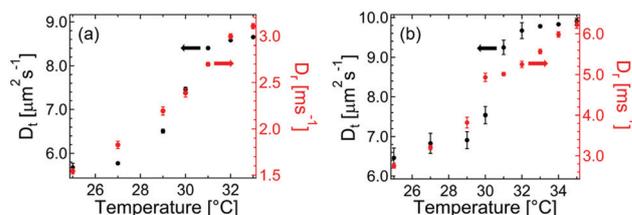Fig. 4 Results from angle-dependent DDLS measurements. $g_{VH}^{(2)}(q,\tau) - 1$ for AuNR–PNIPAM-1 (a) and AuNR–PNIPAM-2 (b). Shown are data recorded for scattering angles between 20° and 140° in 10° steps. The scattering angle increases from blue to red. Representative $g_{VH}^{(2)}(q,\tau) - 1$ at 120° scattering angle for AuNR–PNIPAM-1 (c) and AuNR–PNIPAM-2 (d). The red lines are the corresponding fits to the data using eqn (8).

Fig. 5 Results from temperature dependent DLS and DDLS measurements. Temperature dependence of D_t (black) and D_r (red) for AuNR–PNIPAM-1 (a) and AuNR–PNIPAM-2 (b).

Table 2 Length L, diameter D and aspect ratio p of AuNR cores (values from SAXS) and effective dimensions of the PNIPAM-decorated AuNR–PNIPAM particles using the experimental brush thickness T from DLS experiments of spherical AuNS–PNIPAM reference particles

| | AuNR cores | | | AuNR–PNIPAM-1 | AuNR–PNIPAM-2 |
	AuNR-1	AuNR-2			
L [nm]	76.0 ± 3.7	65.7 ± 3.0	$L + 2T$ [nm]	145 ± 4	135 ± 3
D [nm]	12.4 ± 0.6	10.4 ± 0.6	$D + 2T$ [nm]	81 ± 1	79 ± 1
$p = L/D$	6.1 ± 0.6	6.3 ± 0.7	$p = (L + 2T)/(D + 2T)$	1.8 ± 0.1	1.7 ± 0.1

quality. As the brush thickness T decreases with increasing temperature, there is a reduction in the hydrodynamic particle volume and an increase in the effective aspect ratio. These changes explain the observed increase in D_t and D_r. We will address this aspect in more detail in the following section.

3.3 Comparison to theory

Although the presented light scattering measurements are well suited to determine D_t and D_r with high precision, it is not straightforward to determine the thickness of the PNIPAM brushes on the gold nanorods. This information however is needed to allow for any comparison to theory. Therefore, we chose to measure gold nanospheres that were decorated with the same PNIPAM ligand as an isotropic reference system. Since these particles are only expected to show a contribution from translational diffusion in DLS, it is possible to accurately determine their hydrodynamic radii R_h at different temperatures. The corresponding description of the synthesis and the characterization of these AuNS–PNIPAM particles by TEM, SAXS, DLS and UV/vis spectroscopy can be found in the ESI† (Fig. S17–S20). Using the radius of the gold cores from SAXS (6.89 ± 0.06 nm) and the hydrodynamic radii from DLS, we calculated the brush thickness T for a broad range of temperatures. The respective values are listed in Table S2 in the ESI.† At a temperature of 25 °C, the brush thickness is 34.5 ± 0.1 nm. This value is slightly smaller but still in good agreement to the theoretically calculated thickness of 43.2 nm using the radius of gyration and assuming good solvent conditions. More details about the theoretical calculation are provided in the ESI.† The discrepancy between the theoretical brush thickness and the experimental brush thickness can be explained by the relatively large polydispersity of our ligand. Since the theoretical calculation is based on the average molecular weight and does not take into account the high polydispersity, the theoretical brush thickness is overestimated. For the following considerations we will use the experimental values of T obtained from DLS measurements of our spherical reference particles assuming that the grafting density on the rods is comparable. To calculate the effective aspect ratio of the gold nanorods decorated with the polymer brushes, the experimental values of T are added twice to the length L and the diameter D of the gold nanorod cores obtained from the SAXS experiment. The resulting dimensions and aspect ratios for 25 °C are summarized in Table 2.

Using the estimated total dimensions of the AuNR–PNIPAM particles we calculated the theoretical diffusion coefficients according to eqn (9) and (12). The results are listed in Tables S3 and S4 (ESI†) in direct comparison to the experimentally

determined values. The experimental diffusion coefficients are larger than the theoretically calculated ones for both samples at all temperatures. The deviation is smallest for AuNR–PNIPAM-1 at 25 °C where we find $D_t = 4.82 \pm 0.23$ µm^2 s^{-1} and $D_r = 1.48 \pm 0.27$ ms^{-1} from theory and $D_t = 5.68 \pm 0.10$ µm^2 s^{-1} and $D_r = 1.54 \pm 0.03$ ms^{-1} from experiment. For the slightly shorter particles AuNR–NIPAM-2, we find $D_t = 5.05 \pm 0.29$ µm^2 s^{-1} and $D_r = 1.79 \pm 0.25$ ms^{-1} from theory and $D_t = 6.46 \pm 0.25$ µm^2 s^{-1} and $D_r = 2.75 \pm 0.06$ ms^{-1} from experiment at 25 °C. With increasing temperature the deviation between experiment and theory increases as shown by the corresponding ratios (Exp./Theo.) listed in Tables S3 and S4 (ESI†).

While the theory and experiment are in reasonable agreement, there are some differences, which can be explained as follows:

(1) The dimensions of the AuNR–PNIPAM particles used for the theoretical calculations assume the same brush thickness as experimentally determined for the spherical reference particles. While this is most likely the case for the tips of the gold nanorods where the curvature is comparable to the curvature of the spheres, we expect a different grafting density and brush thickness on the sides of the rods. Thus, the estimated total diameter ($D + 2T$) is only approximate. For example, a reduction in the brush thickness on the sides of 10% (everything else being equal) leads to good agreement with theory at 25 °C. Further studies of the brush thickness as a function of curvature may shed light on this effect.

(2) With increasing temperature the brush thickness decreases, leading to an increase in the effective aspect ratio. Consequently, the theoretical model becomes less appropriate as the particles become less ellipsoidal due to the ligand shell collapse.

In future works it might be interesting to study different molecular weight ligands and different grafting densities assumed that the latter quantity can be precisely determined. We expect the grafting density to have a significant influence on the temperature response of the ligand shell, *i.e.* for higher grafting densities, the collapse of the brush will be less pronounced and *vice versa* for lower grafting densities. With shorter or longer ligands, the effective aspect ratio and also its temperature-dependence will be altered allowing more tunability of the system.

4 Conclusion

We have measured intensity–time autocorrelation functions of gold nanorods decorated with thermoresponsive polymer ligands using dynamic and depolarized dynamic light scattering. Measurements were performed over a broad range of scattering angles to

precisely determine the translational and rotational diffusion coefficients. Experiments at different temperatures approaching the lower critical solution temperature of the polymer ligand were used to study the increase of both diffusion coefficients with temperature. The observed changes are attributed to changes in the overall hydrodynamic particle volume and in the effective aspect ratio due to the collapse of the polymer ligand with increasing temperature. The thickness of the ligand shell and its temperature dependent changes were determined using polymer decorated gold nanoparticles of spherical shape as isotropic reference particles. Using this information, we could theoretically calculate the expected diffusion coefficients for the gold nanorods. Using a model of prolate spheroids we find very good agreement between experiment and theory. Slight deviations were attributed to the relatively large polydispersity of our ligand and potential differences in grafting density and thus brush thickness at the tips of the nanorods as compared to their sides. As the ligand shell collapses in response to an increase in temperature, the theoretical model becomes less suitable to describe the experiment. This observation is explained by the decreasing effective aspect ratio of the particles as the ligand shell collapses. Thus, the particles become less ellipsoidal and more cylindrical with increasing temperature. The ability to tune the aspect ratio offers a unique tool for understanding diffusion of anisotropic particles, and has the potential for a range of applications in colloid science, such as understanding self-assembly processes in suspensions of anisotropic particles.

5 Experimental section

5.1 Materials

Cetyltrimethylammonium bromide (CTAB; VWR Chemicals, $\geq$99%), dimethylformamide (DMF; Aldrich, > 99.8%), 2-(dodecylthiocarbonothioylthio)-2-methylpropanoic acid (DDMAT; Aldrich, >99%), gold(III) chloride trihydrate (HAuCl$_4$; Sigma-Aldrich, $\geq$99.9%), hydroquinone (Roth, $\geq$99.5%), N-isopropylacrylamide (NIPAM; TCI, >98%), silver nitrate (AgNO$_3$; Fluka, $\geq$99.5%), sodium borohydride (NaBH$_4$; Sigma-Aldrich, 99%) and sodium hydroxide (NaOH; Fisher Scientific, UK) were used as received. Water was purified with a Merck Milli-Q system resulting in a final water resistivity of 18 MΩ cm.

5.2 Synthesis

Gold nanorods. Single-crystalline gold nanorods were synthesized using seed mediated growth following the protocol by Vigderman and Zubarev.[11] Single-crystalline gold seeds were synthesized by first preparing an aqueous solution of HAuCl$_4$ (10 mL, 0.5 mM) in 0.1 M CTAB at 30 °C. Secondly, 0.378 mg NaBH$_4$ (0.01 M) was dissolved in 1 mL NaOH (0.01 M) and 0.46 mL of the freshly prepared solution was added under stirring to the HAuCl$_4$ solution at 30 °C. Then, 10 mL of an aqueous solution of HAuCl$_4$ (0.5 mM) in 0.1 M CTAB was prepared and stirred at 30 °C. Following this, 70 µL of an aqueous AgNO$_3$ solution (0.1 M) was added and after slow shaking by hand 0.5 mL of an aqueous hydroquinone solution

(16 mM for AuNR-1, 13 mM for AuNR-2) was added. The solution was shaken by hand until the mixture became clear. Afterwards 0.16 mL of the initial seed solution was added. After 24 hours, the gold nanorods, stabilized by CTAB, were purified by two times of centrifugation for 20 minutes at 5400 rcf each time.

PNIPAM ligand. The linear PNIPAM ligand with terminal trithiocarbonate groups was synthesized by RAFT polymerization following the protocol by Ebeling et al.[26] The resulting number average molecular weight of the ligand was 85 000 g mol^{-1}. Further details can be found in the ESI.†

5.3 Sample preparation

The initial CTAB stabilizer on the surface of the as-prepared AuNR was exchanged by PNIPAM to render the particles with a thermo-responsive polymer shell.[13] For this purpose, 0.46 g of PNIPAM were mixed with 45.9 mL Milli-Q water. 18 mL of the PNIPAM solution was added to AuNR–PNIPAM-1 and 20 mL to AuNR–PNIPAM-2. It is important that an excess of polymer is added to grant the ligand exchange of CTAB to PNIPAM. The samples were purified and centrifuged at 6810 rcf for 90 minutes at 30 °C. The residues were redispersed in water. The purification process was repeated twice. To further enhance the colloidal stability of the samples, additional ligand exchange steps were performed. For this, PNIPAM (0.77 mg for AuNR–PNIPAM-1 and 0.91 mg for AuNR–PNIPAM-2) was dissolved in 0.5 mL water and 0.1 mg of NaBH$_4$ were added to cleave off the trithiocarbonate terminal group and render the ligand with thiol termini. After stirring for 10 minutes, the solution was added to 5 mL of the aqueous gold nanorod samples (0.625 mM). The solutions were stirred for 120 hours and then centrifuged once for 24 hours at 5985 rcf at 20 °C. The residues were dispersed in 5 mL Milli-Q water.

5.4 Methods

Small angle X-ray scattering. SAXS measurements were realised on a XENOCS 2.0 device with sample-to-detector distances of 0.55 and 2.5 m. The beam had a wavelength of 0.15 nm and was collimated to a length of 250 µm. A Pilatus 3 300K detector with a pixel size of 29.584 µm^2 was used for collecting the scattering data. The exposure time for each measurement was 1 h. The q-range was calibrated using the scattering of silver behenate. The samples were filtered with 5 µm PTFE hydrophobic syringe filters and filled into quartz glass mark-tubes (WJM Glas) with an outer diameter of 1 mm previous. Milli-Q water was measured as background. The scattering data was processed, combined and background subtracted using Foxtrot 3.4.9 (Xenoxs, Soleil Synchrotron).

Transmission electron microscopy. Transmission electron microscopy was performed on a JEOL JEM-2100Plus operating in bright-field mode at 80 kV acceleration voltage. Samples were prepared by drop-casting of dilute particle dispersions on carbon-coated copper grids (200 mesh, Science Services). Particle dimensions were obtained using the open source image analysis software ImageJ.

The 2D image series for the electron tomography were recorded in bright-field mode using a high-tilt sample holder. The tilt series was acquired with automatic rectification (corrections of focus and horizontal and vertical displacement) by using the recorder software from the TEMography™ 3-D

Reconstruction software package (System in Frontier, Inc., Tachikawa, TYO, JP) on a 4096 × 4096 pixels Gatan™ OneView camera (Gatan, Inc., Pleasanton, CA, USA). The tilt range was set from −67° to 75° with a basic increment of 1°, giving a total of 142 images. The tilt series data was treated for image processing and reconstruction using the Composer and Visualizer-evo software from the TEMography™ 3-D Reconstruction software package.

(Depolarized) dynamic light scattering. The light scattering experiments were realised on an 3D LS Spectrometer (LS Instruments) operated in 2D mode. A HeNe laser (λ = 632.8 nm) was used as light source and the scattered light was detected by two avalanche photodetectors in pseudo-cross correlation. Samples were prepared in cylindrical quartz glass cuvettes, which were placed in a decalin bath with a controllable temperature device. To select the polarization of the scattered light, Glan–Thompson polarization prisms with an extinction ratio of 10^{-6} were applied. Previous to the analysis, 0.5 mL of the respective AuNR–PNIPAM dispersions was diluted with 1.5 mL Milli-Q water and the pH was adjusted to 7 using a dilute NaOH solution. The solutions were filtered with a 5 μm PTFE hydrophobic syringe filter and added in a quartz glass cuvette.

UV/vis absorbance spectroscopy. Absorbance spectra were recorded with a Specord® S600 from Analytic Jena AG. All measurements were recorded in macro PMMA cuvettes from VWR with a pathlength of 1 cm. Temperature dependent measurements were performed in a Peltier controlled sample changer equipped with a temperature sensor placed in a reference cuvette. Dilute aqueous dispersions were measured in a temperature range from 15 to 33 °C for the AuNR–PNIPAM samples and 15 to 40 °C for the spherical AuNS–PNIPAM reference particles.

Conflicts of interest

There are no conflicts to declare.

Note after first publication

This article replaces the version published on the 10th March 2021, which contained errors in eqn (1).

Acknowledgements

Notes and references

1 R. Nixon-Luke and G. Bryant, *Part. Part. Syst. Charact.*, 2018, **36**, 1800388.

2 U. Kreibig and M. Vollmer, *Optical Properties of Metal Clusters*, Springer, Berlin, 1995.

3 S. A. Maier, M. L. Brongersma, P. G. Kik, S. Meltzer, A. A. G. Requicha and H. A. Atwater, *Adv. Mater.*, 2001, **13**, 1501–1505.

4 E. Ozbay, *Science*, 2006, **311**, 189–193.

5 M. Grzelczak, J. Perez-Juste, P. Mulvaney and L. M. Liz-Marzan, *Chem. Soc. Rev.*, 2008, **37**, 1783–1791.

6 S. J. Tan, M. J. Campolongo, D. Luo and W. L. Cheng, *Nat. Nanotechnol.*, 2011, **6**, 268–276.

7 K. Z. Liu, Z. L. He, J. F. Curtin, H. J. Byrne and F. R. Tian, *Sci. Rep.*, 2019, **9**, 7421.

8 N. G. Bastus, J. Comenge and V. Puntes, *Langmuir*, 2011, **27**, 11098–11105.

9 J. Perez-Juste, I. Pastoriza-Santos, L. M. Liz-Marzan and P. Mulvaney, *Coord. Chem. Rev.*, 2005, **249**, 1870–1901.

10 A. V. Alekseeva, V. A. Bogatyrev, B. N. Khlebtsov, A. G. Mel'nikov, L. A. Dykman and N. G. Khlebtsov, *Colloid J.*, 2006, **68**, 661–678.

11 L. Vigderman and E. R. Zubarev, *Chem. Mater.*, 2013, **25**, 1450–1457.

12 B. Nikoobakht and M. A. El-Sayed, *Chem. Mater.*, 2003, **15**, 1957–1962.

13 T. Honold, D. Skrybeck, K. G. Wagner and M. Karg, *Langmuir*, 2016, **33**, 253–261.

14 N. Carl, J. Sindram, M. Gallei, S. U. Egelhaaf and M. Karg, *Phys. Rev. E*, 2019, **100**, 052605.

15 S. Murphy, S. Jaber, C. Ritchie, M. Karg and P. Mulvaney, *Langmuir*, 2016, **32**, 12497–12503.

16 M. Tagliazucchi, M. G. Blaber, G. C. Schatz, E. A. Weiss and I. Szleifert, *ACS Nano*, 2012, **6**, 8397–8406.

17 M. Karg, S. Jaber, T. Hellweg and P. Mulvaney, *Langmuir*, 2011, **27**, 820–827.

18 D. Lehner, H. Lindner and O. Glatter, *Langmuir*, 2000, **16**, 1689–1695.

19 M. Hoffmann, Y. Lu, M. Schrinner, M. Ballauff and L. Harnau, *J. Phys. Chem. B*, 2008, **112**, 14843–14850.

20 M. Glidden and M. Muschol, *J. Phys. Chem. C*, 2012, **116**, 8128–8137.

21 J. Rodríguez-Fernández, J. Pérez-Juste, L. M. Liz-Marzán and P. R. Lang, *J. Phys. Chem. C*, 2007, **111**, 5020–5025.

22 B. J. Berne and R. Pecora, *Dynamic Light Scattering: With Applications to Chemistry, Biology and Physics*, Dover Publications, New York, 1976.

23 M. A. M. Tirado and J. G. A. de la Torre, *J. Chem. Phys.*, 1980, **73**, 1986–1993.

24 M. M. Tirado and J. G. A. de la Torre, *J. Chem. Phys.*, 1979, **71**, 2581–2587.

25 F. J. Perrin, *J. Phys. Radium*, 1936, **7**, 1–11.

26 B. Ebeling and P. Vana, *Macromolecules*, 2013, **46**, 4862–4871.